Ultrasonics 53 (2013) 350–362

Contents lists available at SciVerse ScienceDirect

Ultrasonics

journal homepage: www.elsevier.com/locate/ultras

Modeling elastic waves in coupled media: Estimate of soft tissue influence and application to quantitative ultrasound

Jiangang Chen [a,1], Li Cheng [a], Zhongqing Su [a,*], Ling Qin [b]

[a] Department of Mechanical Engineering, The Hong Kong Polytechnic University, Kowloon, Hong Kong Special Administrative Region
[b] Musculoskeletal Research Laboratory, Department of Orthopaedics and Traumatology, The Chinese University of Hong Kong, New Territories, Hong Kong Special Administrative Region

ARTICLE INFO

Article history:
Received 24 April 2012
Received in revised form 25 June 2012
Accepted 29 June 2012
Available online 14 July 2012

Keywords:
Quantitative ultrasound (QUS)
Coupling effect
Soft tissues
First-arriving signal (FAS)
Second-arriving signal (SAS)

ABSTRACT

The effect of medium coupling on propagation of elastic waves is a general concern in a variety of engineering and bio-medical applications. Although some theories and analytical models are available for describing waves in multi-layered engineering structures, they do not focus on canvassing ultrasonic waves in human bones with coupled soft tissues, where the considerable differences in acoustic impedance between bone and soft tissue may pose a challenge in using these models (the soft tissues having an acoustic impedance around 80% less than that of a typical bone). Without proper treatment of this coupling effect, the precision of quantitative ultrasound (QUS) for clinical bone assessment can be compromised. The coupling effect of mimicked soft tissues on the first-arriving signal (FAS) and second-arriving signal (SAS) in a series of synthesized soft-tissue–bone phantoms was investigated experimentally and calibrated quantitatively. Understanding of the underlying mechanism of the coupling effect was supplemented by a dedicated finite element analysis. As revealed, the medium coupling impacts influence on different wave modes to different degrees: for FAS and SAS, the most significant changes take place when the soft tissues are initially introduced, and the decrease in signal peak energy continues with increase in the thickness or elastic modulus of the soft tissues, but the changes in propagation velocity fluctuate within 5% regardless of further increase in the thickness or elastic modulus of the soft tissues. As an application, the calibrated effects were employed to enhance the precision of SAS-based QUS when used for predicting the simulated healing status of a mimicked bone fracture, to find prediction of healing progress of bone fracture based on changes in velocity of the FAS or the SAS is inaccurate without taking into account the effect of soft tissue coupling, entailing appropriate compensation for the coupling effect.

1. Introduction

As a consequence of medium coupling, elastic waves in a multi-medium system behave differently from their counterparts in homogeneous media, presenting somewhat subtle and unique features. This phenomenon has raised a concern in various applications, as typified by elastic-wave-based nondestructive evaluation (NDE) for multi-layered engineering structures (*e.g.*, submerged oil pipelines or turbine blades with plasma spray) and quantitative ultrasound (QUS)-based bone assessment in the clinic. It is appreciated that such medium coupling effects should ideally be rectified, to enhance the precision of these NDE and QUS applications [1,2]. Addressing this concern, a number of theoretical and analytical models [3–8], as well as some commercial tools (*e.g.*, DISPERSE®, Imperial College London, UK), have been established, capable of describing the propagation characteristics of elastic waves in multi-layered structures.

However, it is envisaged that most of these available models and tools were not specially developed for the applications in which different components of the medium have considerably distinct material, acoustic and physical properties (*e.g.*, one has much higher Young's modulus than the other). An example that best reflects this contrast is the biological bone system, a multi-layered system consisting of hard bones and soft tissues (skin, muscle, marrow, *etc.*), in which the soft tissues have the acoustic impedance around 80% less than that of a typical bone. When QUS is implemented for bone assessment *in vivo*, apart from the degenerative disorders of bone, the coupled soft tissues modulate ultrasound waves as well, to different extents for different wave modes [9,10]. Previous study [11] has demonstrated that soft tissues can affect wave propagation in bones, manifesting as (i) changes in the measured wave velocities and magnitudes, due to the longer wave propagation path, wave leakage, uneven thickness

* Corresponding author. Fax: +852 2365 4703.
E-mail address: MMSU@polyu.edu.hk (Z. Su).
[1] Present address: The Ultrasound and Elasticity Imaging Laboratory, Department of Biomedical Engineering, Columbia University, New York, NY, USA.

0041-624X/$ - see front matter © 2012 Elsevier B.V. All rights reserved.
http://dx.doi.org/10.1016/j.ultras.2012.06.018

or inhomogeneity of the soft tissues; and (ii) the coupling between different wave modes.

Nevertheless, these coupling effects are often ignored in clinical practice, and explanation of captured wave signals is simply based on the theorem of elastic waves in single-medium solids in a free state. Failing to differentiate the influence of coupled soft tissues from that due to the degradation in bone can prevent QUS delivering precise results. When exploring the coupling effect of a soft medium on wave propagation in solid structures, most studies have hypothesized that the soft tissues could be simulated using a layer of fluid (*e.g.*, water or 98% glycerin), because of the morphologic similarity between the fluid and human soft tissues in many respects, such as the close ultrasonic attenuation ratio (circa. 0.2 dB/cm at 1 MHz). Yapura and Kinra [5] analytically examined waves in a fluid–solid coupled bi-layer system, reaching the conclusion that the surrounding fluid prominently alters wave propagation. Moilanen et al. [9] experimentally interrogated ultrasonic waves in a bi-layer structure designed to mimic soft tissue-coupled bone, and observed a similar coupling influence from the surrounding fluid on ultrasound waves. White and Wenzel [12] demonstrated that waves in a membrane loaded on one side with a layer of fluid were different from those in a free membrane. Extending the above studies from plates to tubular structures, Cheeke et al. [13] canvassed elastic waves in a thin-walled tube filled with fluid, demonstrating a decrease in wave speed compared with elastic waves in a dry tube. These studies drew much attention to the effect of soft medium coupling on ultrasound waves.

Real human soft tissues are not a fluid layer, however, but a sort of soft substance that can support complex wave propagation, making many of the available fluid–solid bi-layer models inapplicable when used to precisely describe all wave modes in bone. With that constraint, calibration of the influence of the coupled soft medium on ultrasound waves in bones remains significant, but challenging due to the lack of analytical models and methodologies that are able to accurately depict wave propagation in a coupled system consisting of phases with considerably distinct material and physical properties. Applications of QUS in clinical practice without rectification and compensation for such coupling effect may take the risk delivering inaccurate assessment results [14].

It is the above-mentioned deficiencies of current QUS for clinical bone assessment that have motivated the present work. In this study, the propagation characteristics of different wave modes, including the first-arriving signal (defined as FAS hereinafter) and second-arriving signal (SAS hereinafter), propagating in a series of synthesized bone phantoms coupled with mimicked soft tissues, were examined ultrasonically. Quantitative correlations between the changes in FAS/SAS and the variations in coupled soft tissues were achieved. Artificial silicone rubber (defined as ASR thereinafter), a sort of *tissue equivalent material* (TEM), was fabricated to mimic human soft tissues [15]. In light of the limitations of most available analytical models and tools, *in vitro* testing was carried out, wherein the coupling effect was calibrated quantitatively for ASR layers of different thicknesses or elastic moduli (mimicking different *in vivo* conditions of human soft tissues). Understanding of the experimental observations was supplemented with three-dimensional (3D) finite element (FE) analysis. As an application, the calibration results were employed to enhance the precision of SAS-based QUS when used to predict the simulated healing status of a mimicked bone fracture.

2. Coupling effect of soft tissues on QUS

Increasing demand for bone assessment without the use of hazardous ionizing radiation has spurred rapid development of QUS in recent years. Most QUS techniques in clinic are substantially based on examining the FAS, *i.e.*, the wave mode captured first by a receiver placed at a skeletal site. By benchmarking signals collected from a healthy group, changes in FAS can be linked to various pathological disorders of bone [10]. For example, changes in the speed-of-sound or broadband-ultrasound-attenuation of FAS can serve as symptomatic indicators for hip fracture [16].

In spite of its popularity, FAS-based QUS has been increasingly challenged in terms of the precision it can offer, because of the relatively large wavelength of FAS (from a few hundred micrometers to a few millimeters in the normal working frequency range of 0.25–2 MHz). That is because the wavelength of a diagnostic wave should ideally be lower than or equal to the characteristic dimension of the abnormality, as demonstrated elsewhere [17]. This is particularly crucial when QUS is used to monitor callus growth during the healing progress of a fractured bone or to explore local bone characteristics in detail. Certainly it is possible to increase the excitation frequency so as to achieve a reduced wavelength, but this comes with the expense of rapid wave attenuation and therefore compromises diagnostic capacity.

More recently, some researchers [9,18–21] have explored the alternative wave modes that follow the FAS, taking advantage of their shorter wavelengths (*e.g.*, circa. 8 mm at 200 kHz in a cortical bone with a thickness of 4.75 mm [18]) than that of the FAS (around 15 mm in the same bone and at the same excitation frequency [18]) at a given excitation frequency. Of particular interest are transverse wave modes such as the SAS, the wave mode immediately following the FAS. Featuring a shorter wavelength at a given excitation frequency, the SAS has higher sensitivity than the FAS to pathological changes in bone such as degradation in density or reduction in cortical thickness. For example, a test conducted on the tibiae of pubertal girls [22] revealed that different velocities of the SAS can reflect different cortical thicknesses, reinforcing the potential of using the SAS as an indicator for the diagnosis of osteoporosis (in osteoporotic patients the tibial cortex can be thinner (around 90% than normal) due to osteoporotic endosteal resorption [23]).

However, the application of QUS to *in vivo* clinical bone assessment, whether using FAS or SAS, has been handicapped to some extent because ultrasound waves are susceptible to the surrounding soft tissues (skin, muscle, marrow, *etc.*) [9,14]. Apart from bone degradation, coupled soft tissues also modulate ultrasound waves, preventing QUS from delivering precise assessment if such effects are ignored. This diminishes the reliability of QUS when used *in vivo*. To tackle this problem, continued efforts have been made to somehow eliminate the coupling effect of soft tissues by carefully maneuvering transducers. For instance, a device comprised of a transmitter and a receiver was invented [9]. By fixing the transmitter and then moving the receiver in constant steps, signals captured at each step contributed to a distance–time diagram, from which the wave propagation velocities could be determined without interference from the overlying soft tissues. Another development was a bidirectional probe consisting of two groups of emitters surrounding another group of 14 receivers [24]. Ultrasound waves generated by the two emitters traveled along the bone in opposite directions, and were then received by the receivers. By taking into account the time delays of waves propagating in opposite directions, errors arising from unequal thicknesses of the coupled soft tissues and the probe inclination could be rectified.

Although most of the current endeavors have focused on the development of ingenious transducers or the introduction of innovative calculation algorithms to minimize the coupling effect, insight into the underlying mechanism of the coupling effect of soft tissues on ultrasound waves in bone structures is of vital importance, but relevant studies are lacking. Quantitative calibration and appropriate compensation for this effect are obviously

significant. It is noteworthy that, although this study addresses a bio-medical challenge, its underlying essence is still a problem in the discipline of solid mechanics: *elastic wave propagation in coupled media*.

3. Ultrasound waves in bone structures

Human long bones (*e.g.*, the distal radius or femur) are complex tubular structures with irregular cross-sections along the bone axis, which are overlaid with soft tissues including muscles and skin, and filled with marrow. Given the fact that the transmitter and receiver placed in tandem in axial transmission-based QUS are a short distance apart (20–50 mm), the part of the bone covered by this transmitter–receiver pair can be hypothesized to be locally flat, neglecting its curvature [9,22]. That assumption is not expected to undermine the precision of the current analysis on the coupling effect. Under this circumstance, bone-guided ultrasound waves can be defined using the *theory of elastic waves* in thin plates, *i.e.*, *Lamb waves* (the modality of elastic waves in a thin plate or shell with the wavelength being of the order of the thickness of the plate or shell [7]). In the theory, Lamb waves comprise two mode groups: *symmetric* and *anti-symmetric* modes, denoted by S_i and A_i ($i = 0, 1\ldots$), respectively, with their subscripts being the wave mode order. The two groups can be described by [7]

$$\frac{\tan(qh)}{\tan(ph)} = -\frac{4k^2qp}{(k^2-q^2)^2} \quad \textit{for symmetric modes}, \tag{1a}$$

$$\frac{\tan(qh)}{\tan(ph)} = -\frac{(k^2-q^2)^2}{4k^2qp} \quad \textit{for anti}-\textit{symmetric modes}, \tag{1b}$$

where

$$p^2 = \frac{\omega^2}{c_L^2} - k^2, q^2 = \frac{\omega^2}{c_T^2} - k^2, k = \frac{2\pi}{\lambda},$$

$$c_L = \sqrt{\frac{E(1-\nu)}{\rho(1+\nu)(1-2\nu)}}, \text{ and } c_T = \sqrt{\frac{E}{2\rho(1+\nu)}}$$

In the above h, E, ρ, ν, k, ω and λ are the half thickness, elastic modulus, density and Poisson's ratio of the plate, wavenumber, circular frequency and wavelength of the wave mode, respectively. c_L and c_T are the velocities of the longitudinal and transverse (shear) wave modes in the plate, respectively. In particular, S_0 and A_0 are the lowest-order modes in the two groups, respectively. At a given frequency, S_0 and A_0 co-exist and higher-order modes appear as frequency increases.

With the above hypothesis, the FAS in bone structures corresponds to the S_0 mode, propagating with the greatest velocity among all the guided wave modes in the bone (in a relatively low frequency range) and arriving at a receiver first. Like S_0, particles in the FAS have predominantly radial in-plane movements. On the other hand, the SAS in bone structures, a shear vertical (SV) mode, is equivalent to the A_0 mode, having a predominantly out-of-plane (vertical to the plate surface) particulate motion pattern [25]. The propagation characteristics of Lamb waves in isotropic and homogeneous elastic plate consisting of multiple solid layers (solids–solids) can be well described using the above wave theories. Further, with additional constraints, these theories can be extended to depict the FAS and SAS in human bone structures, provided the coupled soft tissues are treated as a layer of fluid (a fluid–solid bi-layer system) [9,26,27]. It is relevant to note that the major difference between elastic waves in a solid–solid system and in a fluid–solid system lies in the fact that the solid layers of the former system supports the propagation of in-plane wave modes whereas the fluid layer of the latter does not, because a fluid layer can support only out-of-plane particulate motion. The coupling between two media in a fluid–solid bi-layer system introduces extra constraints to particulate motion at the interface (compared with a free status, *i.e.*, single phase), providing a radiation path for Lamb waves in the solids to leak into surrounding media, forming *leaky Lamb waves* [20]. When leaky Lamb waves encounter boundaries of different media, they are scattered and reverberate throughout the whole system, accompanied by mode conversion. With this complexity, as well as the dispersive and multimodal nature of FAS and SAS, it is often a challenge to analytically describe waves in real soft-tissue-coupled bone structures.

Considering a fluid–solid-coupled layer of infinite extent, the characteristic equation for this bi-layer system can be defined, if both solid and fluid are deemed isotropic, as [9]

$$\det(G(\omega, k, c_F, c_L, c_T, a, h, \rho_F, \rho)) = 0, \tag{2}$$

where G is the characteristic matrix; a and h are the thickness of the fluid layer and half thickness of the solid layer, respectively; ρ and ρ_F are the densities of the solid and fluid layers, respectively; c_F is the bulk wave velocity in fluid. Solutions to Eq. (2) depict the dispersion properties of different wave modes in a fluid–solid bi-layer system.

Even so, it must be envisaged that

(i) Most existing models and analytical tools were not specially developed for multi-layered systems in which the mutually coupled media have properties that are quite different from each other, for example the human bone structures (soft tissues being '*soft*' and in the order of kPa, whereas bone '*hard*' and in the order of GPa); and
(ii) Real human soft tissues are not a fluid but a soft substance that supports complex wave propagation. When applied to real bone structures, these models and tools often present certain limitations.

Under such circumstances, *in vitro* testing, supplemented by dedicated finite element simulation, still has advantages in faithfully canvassing the effect of soft tissue coupling on the FAS and SAS in bone structures.

4. Sample preparation for *in vitro* testing: synthesized soft-tissue–bone phantoms

For *in vitro* testing, a series of soft-tissue–bone phantoms was fabricated (as listed in Table 1), each of which comprised a bone-mimicking hard phase using an acrylic plate ($460 \times 240 \times 3.2$ mm^3) and a soft-tissue-mimicking soft phase using an artificial silicone rubber (ASR) layer (in-plane dimension: 160×60 mm^3). Due to its similarity in material and mechanical properties to real bones [9], acrylic, a kind of prevailing bone-mimicking material, has been widely used to imitate cancellous and cortical bones (*e.g.*, density: $\rho_{acrylic} = 1.2$ g/cm^3 *vs.* $\rho_{real\ bone} \approx 1.5$ g/cm^3; elastic modulus: $E_{acrylic} = 4.24$ GPa *vs.* $E_{real\ bone} \approx 2 \sim 20$ GPa [28]; Acoustic impedance: $Z_{acrylic} = 2.26$ MPa · s/m *vs.* $Z_{real\ bone} \approx 1.7 \sim 5.5$ MPa · s/m; Poisson's ratio: $\nu_{acrylic} = 0.39$ *vs.* $\nu_{real\ bone} \approx 0.37$). Acrylic can easily be tailored to accommodate various bone geometries. On the other hand, ASR, considered a sort of TEM, has comparability to human soft tissues, owing to the morphologic similarity [29].

Various ASR layers were prepared to feature (i) the same elastic properties ($E_{ASR} = 11.96$ kPa, similar to that of typical healthy 2human soft tissues [30], and density: $\rho_{ASR} = 1.075$ g/cm^3 *vs.* $\rho_{real\ human\ soft\ tissue} = 1.0$ g/cm^3 [31]) but different thicknesses (0.8–9.4 mm, covering the thickness range of human soft tissues at major skeletal sites); or (ii) the same thickness (3.4 mm) but different elastic properties ($E_{ASR} = 2.89 \sim 536.51$ kPa, in a range from normal to pathological conditions of human soft tissues). ASRs with

Table 1
Description of synthesised soft-tissue–bone phantoms.

Sample	Thickness of ASR (mm)	Elastic modulus of ASR (kPa)	ROS
0# (no ASR)	0	N.A.	N.A.
ASR having different thicknesses			
T1#	0.8	11.96	1.6
T2#	1.9	11.96	1.6
T3#	3.4	11.96	1.6
T4#	4.2	11.96	1.6
T5#	5.1	11.96	1.6
T6#	6.3	11.96	1.6
T7#	7.7	11.96	1.6
T8#	9.4	11.96	1.6
ASR having different elastic moduli			
E1#	3.4	2.89	2.0
E2#	3.4	6.86	1.8
E3#	3.4	11.96	1.6
E4#	3.4	19.65	1.4
E5#	3.4	32.38	1.2
E6#	3.4	55.87	1.0
E7#	3.4	73.41	0.8
E8#	3.4	119.62	0.6
E9#	3.4	181.23	0.4
E10#	3.4	336.87	0.2
E11#	3.4	536.51	0

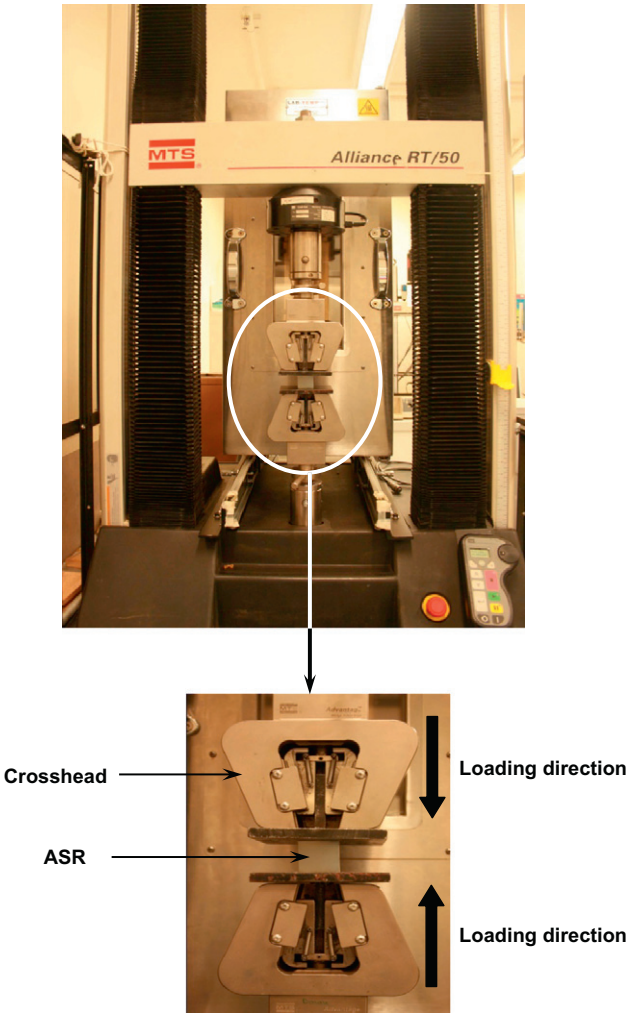

Fig. 1. Compression testing for fabricated ASR (on MTS® RT/50 testing platform).

different elastic properties were fabricated by controlling the proportions of silicone gel, firming agent and oil in the mixture, as described in the Appendix. Different ratios of oil to silicone gel (ROS) led to different elastic moduli of the resulting ASR (the lower the ROS the higher the elastic modulus). Each ASR was adhered to a bone-mimicking hard phase using an adhesive specifically developed for silicone rubber (a water-like glue with little viscosity, able to provide an even, firm and durable adhesion between soft and hard materials through an adhesive layer of about 25 μm), to form a synthesized soft-tissue–bone phantom.

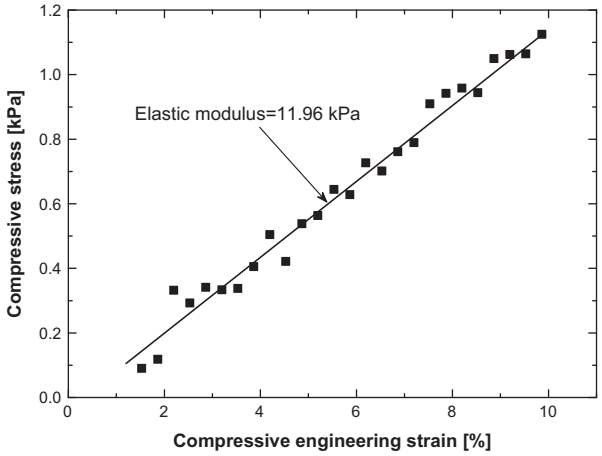

Fig. 2. Stress–strain relationship of fabricated ASR (ROS: 1.6) obtained through the compression testing.

To ascertain the mechanical properties of the fabricated ASR a standard compression test was carried out on a tensile testing platform (MTS® Alliance RT/50) shown in Fig. 1. Uniform compressive loads at a speed of 0.2 mm/s were applied on the ASR (prepared in accordance with the fabrication procedures described in the Appendix) until their axial strains reached 10%. The stress–strain relationship obtained when ROS was 1.6 as a typical example is shown in Fig. 2. It can be seen that the fabricated ASR exhibited approximately linear elastic properties in a deformation range of up to 10%.

5. *In vitro* calibration

5.1. Methodology

The propagation characteristics of the FAS and SAS in the synthesized phantoms were canvassed *in vitro*. All the phantoms were clamped on their four edges on an optical testing table (NEWPORT® ST-UT2). Two waterproof ultrasound transducers (Panametrics-NDTTM-V303-SU; central frequency: 1 MHz; nominal diameter: 13 mm), serving as wave transmitter and receiver, respectively, were collocated at the interface of the soft and hard phases, in conformity to the axial transmission measurement, as shown schematically in Fig. 3a. The transducer pair was instrumented with a signal generation/acquisition system [32], Fig. 3b. The incident diagnostic signal was five-cycle *Hanning*-windowed sinusoidal tonebursts, generated by an arbitrary waveform generation unit (Agilent® E1441). In most QUS implementations, a pulse of a voltage up to a few hundred volts with a narrow bandwidth is often used as the diagnostic signal, so as to achieve energy concentration for driving transmitters to activate ultrasonic waves capable of penetrating thick soft tissues. The captured signals, though with certain tolerance to measurement noise, often include numerous dispersive wave modes spanning a wide frequency range, complicating signal interpretation. The current selection of *Hanning*-windowed tonebursts at a mono-frequency could prevent wave dispersion, and therefore the subsequent signal

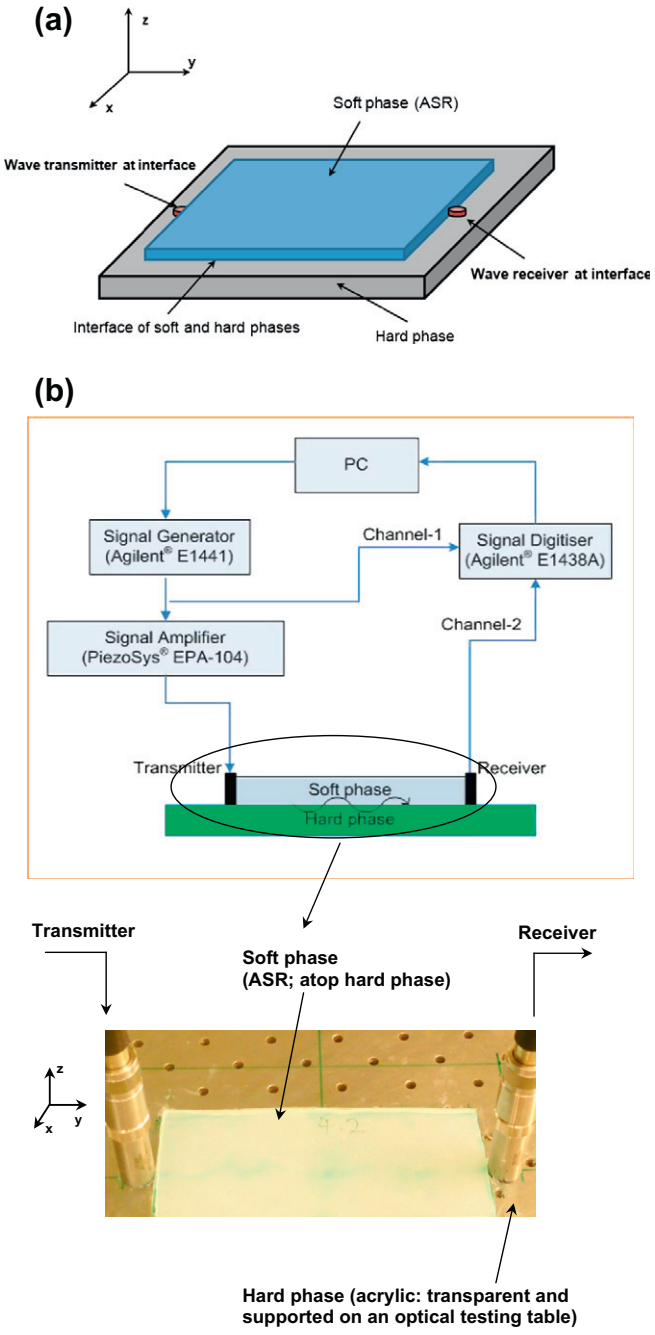

Fig. 3. (a) Schematic description of the synthesised soft tissue-bone phantom; and (b) experimental setup.

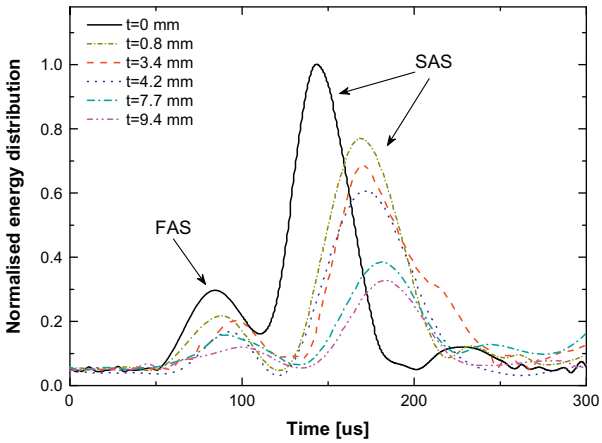

Fig. 4. HT-processed results of *in vitro* signals captured from phantoms without (sample no. 0# ($t = 0$)) and with a coupled ASR layer of different thicknesses (samples no. T1# ($t = 0.8$ mm), T3# ($t = 3.4$ mm), T4# ($t = 4.2$ mm), T7# ($t = 7.7$ mm) and T8# ($t = 9.4$ mm)) (t: thickness of ASR layer; signal being normalized relative to the amplitude extremum of signal in sample no. 0#).

interpretation could be conducted at the excitation frequency. The diagnostic signal was then amplified to 180 $V_{p\text{-}p}$ (peak-to-peak) with a linear amplifier (PiezoSys® EPA-104) to drive the transmitter. Signals were captured with the receiver through a signal digitizer (Agilent® E1438A) at a sampling rate of 25 MHz.

It is in particular noteworthy that, aimed at exploring the coupling effect of mimicked soft tissues on the FAS and SAS in hard phases, the transducer pair was intentionally positioned at the interface of two phases, rather than atop the soft phase, which was different from the actual clinical implementation of QUS. A comparative test (detailed in Section 5.6) demonstrated that when the soft tissue layer is of small thickness, the velocities of the FAS and SAS captured at the interface and those captured atop the soft phase are identical (but not the signal magnitude, as detailed in Section 5.6), because the time-of-flights used for both waves modes to pass through the thin soft tissue layer are negligible (compared with the distance of wave propagation in the bone).

5.2. Coupling effect of ASR with different thicknesses

Both FAS and SAS in sample 0# and T1# to T8# were captured using the described *in vitro* testing method. Diagnostic signals were activated at a series of candidate frequencies from 50 to 200 kHz with a step of 50 kHz, from which the 75 kHz was selected due to the superior identifiability of both wave modes under that excitation frequency. As some representative results, the Hilbert transform (HT)-processed [1] *in vitro* signals, when the thickness of the ASR layer was 0.8 mm (sample T1#), 3.4 mm (sample T3#), 4.2 mm (sample T4#), 7.7 mm (sample T7#) and 9.4 mm (sample T8#), are combined in Fig. 4 for comparison. Included in the figure is also the HT-processed signal in the absence of the ASR layer (sample 0#). The first and second energy concentrations in all signals are associated with the FAS and SAS, respectively. It is evident that the FAS or SAS behaved differently in the absence and presence of a coupled ASR layer; and the extent of such difference was subject to the thickness of the ASR layer. Furthermore, including all the discussed thicknesses (0.8–9.4 mm), *in vitro* measured velocities of FAS and SAS, and their peak energy magnitudes, subject to different thicknesses of the coupled ASR layer, are summarized in Figs. 5 and 6, respectively. In these figures, to facilitate comparative evaluation against wavelength, the thickness of the ASR layer was normalized with regard to the wavelength of the respective wave mode.

Figs. 4–6 reinforce that a coupled ASR layer exerts influence on both the FAS and the SAS, manifesting as a decrease in propagation velocity (from 2.23 km/s to around 2 km/s for FAS and from 1.28 km/s to circa. 1 km/s for SAS, as shown in Fig. 5) and a reduction in signal energy (continuously reduce to around 25% of the magnitude in the phantom without ASR for both FAS and SAS, as indicated in Fig. 6). This influence is evident to distinct extents for different wave modes. For both modes, the most significant changes take place when the ASR layer is initially introduced; then, the decrease in signal peak energy continues as ASR thickness increases, but velocities fluctuate slightly (within 5%) despite further increase of ASR thickness.

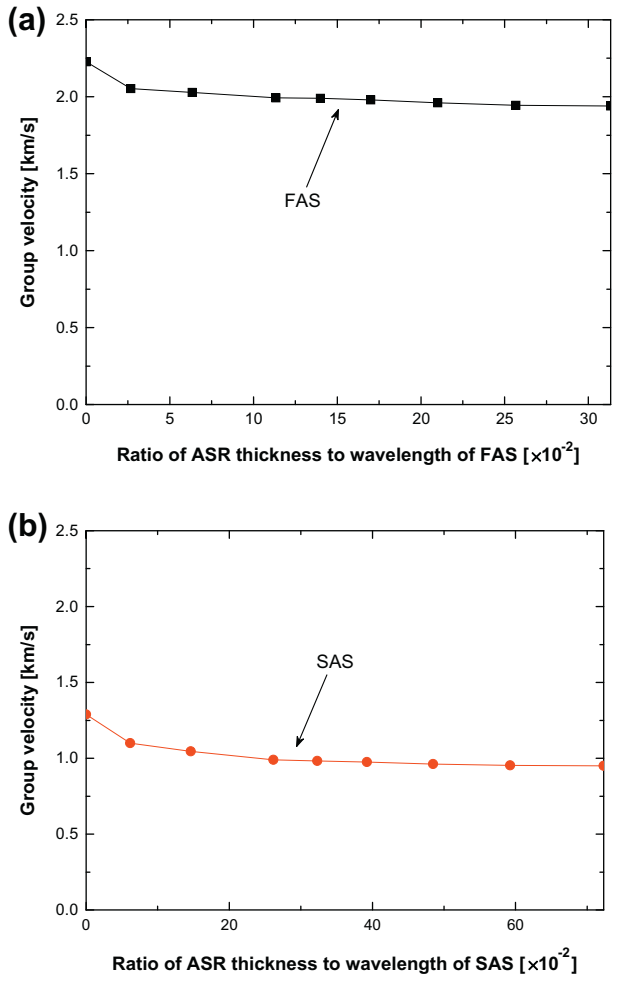

Fig. 5. Group velocities of (a) FAS and (b) SAS in phantoms (samples no. 0#, T1#–T8#) *vs.* ratio of ASR thickness to wavelength.

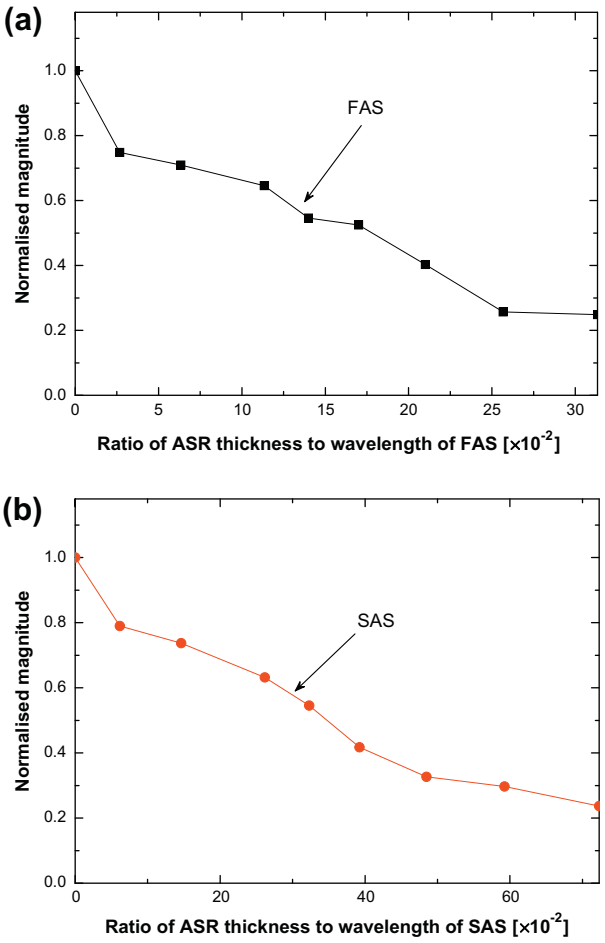

Fig. 6. Magnitudes of (a) FAS and (b) SAS in phantoms (samples no. 0#, T1#–T8#) *vs.* ratio of ASR thickness to wavelength (signal magnitude being normalized relative to the amplitude extremum of signal in sample no. 0#).

5.3. Coupling effect of ASR with different elastic properties

Under the selected excitation frequency (75 kHz), the FAS and SAS were acquired in sample E1#–E11#. Different elastic moduli of the ASR simulated various pathological conditions of human soft tissues, such as scars and burns, which may feature different elastic properties. Including all the moduli under investigation ($E_{ASR} = 2.89 \sim 536.51$ kPa), the *in vitro* measured propagation velocities of the FAS and SAS, and their peak energy magnitudes, subject to different elastic moduli of the coupled ASR layer, are shown in Figs. 7 and 8, respectively, to illustrate the similar variation trends as those observed with different thicknesses of the ASR layer as detailed in Section 5.2. In Fig. 7, the velocity of both modes drops immediately upon introduction of the ASR layer, but subsequently changes slightly with further increase in ASR elastic modulus; in Fig. 8, the peak energy magnitudes of both modes are observed to be continuously attenuated as the modulus increases.

5.4. Dispersion properties

Extending the above *in vitro* measurement by sweeping the excitation frequency from 50 to 200 kHz with a step of 50 kHz, the dispersion properties of the FAS and SAS in different phantoms under the effect of ASR coupling were calibrated. In this study, the frequency range of 50–200 kHz was chosen, including those used in some typical QUS exercises (*e.g.*, 200 kHz in [22] and 100 kHz in [33]). The wavelength of the discussed wave mode in the soft tissue ranges from 7 (at 200 kHz) to 30 mm (at 50 kHz), comparable to the thicknesses of the soft tissue layer (0.8–9.7 mm). Fig. 9 shows the dispersion curves obtained for two wave modes without (sample 0#) and with a coupled ASR layer 3.4 mm in thickness (sample T3#) as an example. The dispersion curves further illustrate that ASR exerts a noticeable coupling effect on the FAS and SAS in bone phantoms compared with their counterparts in a free solid structure without any coupled soft medium.

5.5. Wave mode dominance

Under different excitation frequencies, the FAS and SAS were found to take different proportions of the overall signal energy. This dependence of energy share for a particular wave mode on excitation frequency is called *wave mode dominance* in this study; and the frequency at which a specific wave mode achieves its maximum dominance over the others is called *characteristic frequency* for this mode. By way of illustration, the *in vitro* captured energy magnitudes of the FAS and SAS without (sample 0#) and with a coupled ASR layer 3.4 mm in thickness (sample T3#) as an example, subject to different excitation frequencies, are diagrammed in Fig. 10a and b, respectively.

It can be seen that (i) the FAS achieves the maximum wave mode dominance at circa. 150 kHz (*characteristic frequency* for FAS) and the SAS at 110 kHz (*characteristic frequency* for SAS); and (ii) comparing Fig. 10a and b, the existence of a coupled soft

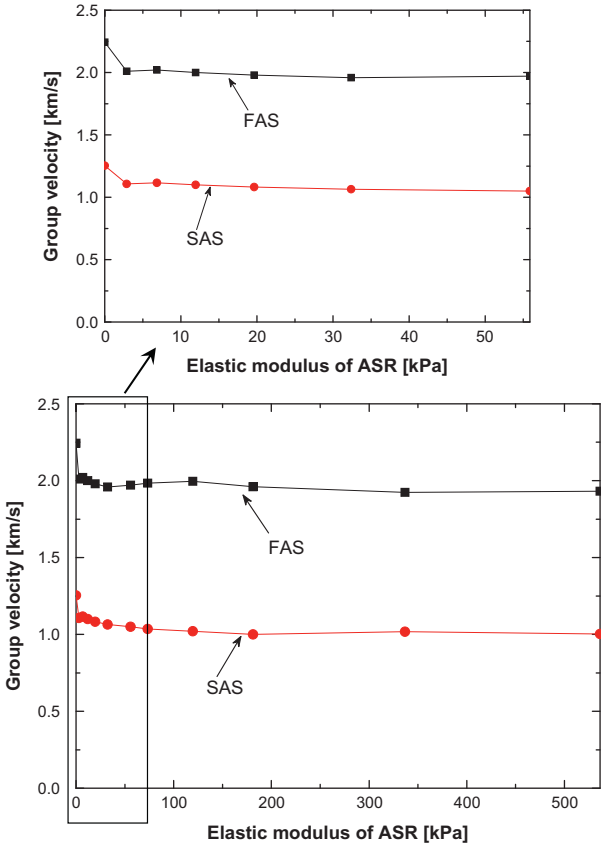

Fig. 7. Group velocities of FAS and SAS in phantoms (samples No. 0#, E1#–E11#) *vs.* elastic modulus of ASR (insert: zoomed-in part showing initial change).

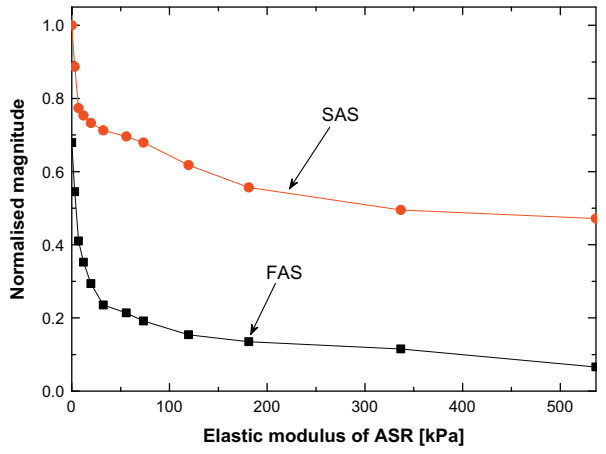

Fig. 8. Magnitudes of (a) FAS and (b) SAS in phantoms (samples no. 0#, E1#–E11#) *vs.* elastic modulus of ASR (signal magnitude being normalized relative to the amplitude extremum of signal in sample no. 0#).

medium does NOT shift these characteristic frequencies, but attenuates energy magnitude. These conclusions may be helpful in clinical practice for selection of the optimal excitation frequency for a diagnostic wave, to have the maximum output of the preferred wave with weak noise influence.

5.6. Discussion of measurement configuration

As stated in Section 5.1, aimed at exploring the coupling effect of soft phase on wave propagation in hard phase, the transducer

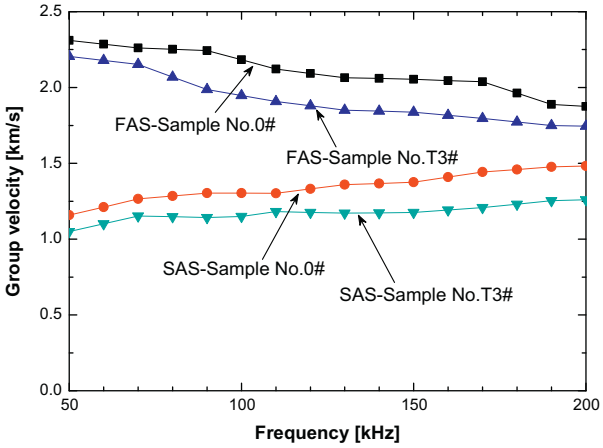

Fig. 9. Dispersion curves for FAS and SAS in phantoms without (sample no. 0#) and with a coupled ASR layer (sample no. T3#).

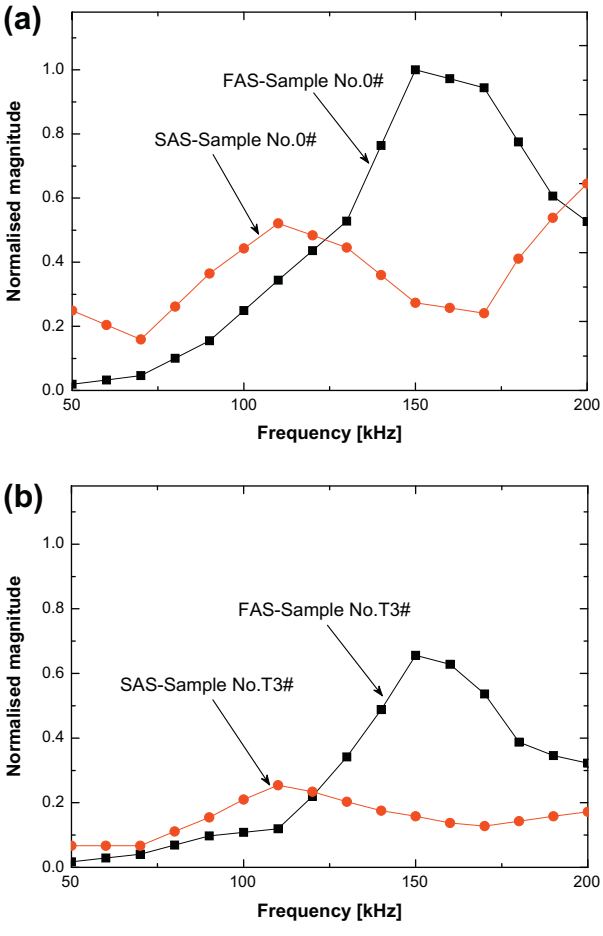

Fig. 10. Wave mode dominance: magnitudes of FAS and SAS in phantoms (a) without (sample no. 0#); and (b) with a coupled ASR layer (sample no. T3#) *vs.* excitation frequency (signal magnitude being normalized relative to the amplitude extremum of signal in sample no. 0# at 150 kHz).

pair was deliberately positioned at the interface of two phases, rather than atop the soft phase (as in clinical practice). To examine the difference between these two measurement configurations, a comparative test was carried out, in which the FAS and SAS were captured when (i) both transducers were collocated at the interface of two phases, as shown schematically in Fig. 11a; and (ii)

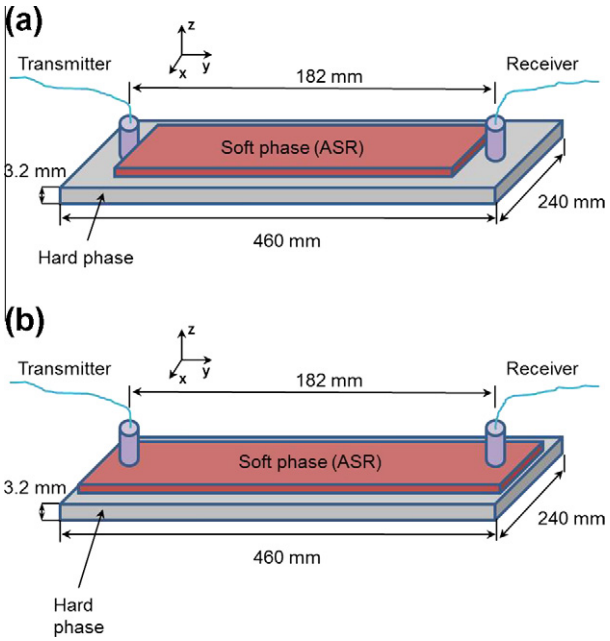

Fig. 11. Schematic illustration of two different measurement configurations with the transmitter and receiver placed (a) at the interface of soft and hard phases; and (b) atop the soft phase.

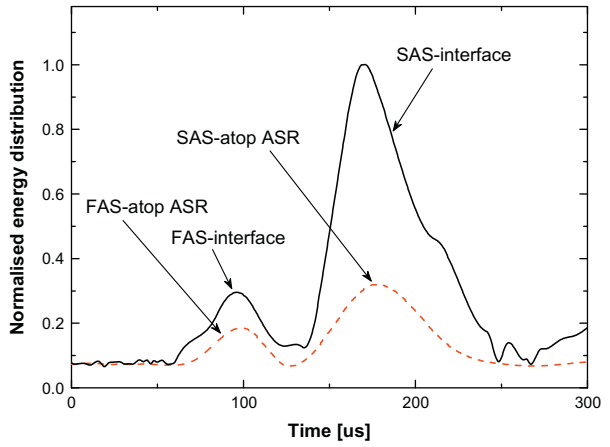

Fig. 12. Comparison of HT-processed results of signals captured under two different measurement configurations in Fig. 11.

both transducers were placed atop the soft phase, Fig. 11b. The same ASR layer ($E_{ASR} = 11.96$ kPa; thickness: 3.4 mm) was used in both configurations, and the distance between transmitter and receiver was kept constant (182 mm).

The HT-processed signals captured under the two configurations are compared in Fig. 12. It can be seen that, for both FAS and SAS, the arrival time remains the same (no change in propagation velocity) regardless of whether the signal is captured at the interface or atop the soft phase. On the other hand, the magnitudes of the peak energy of both modes are much attenuated if the signals are captured atop the soft phase. The conclusion can therefore be drawn that any discrepancy between the propagation velocities of the FAS and SAS, when acquired at the interface or atop the soft tissue, can be ignored, provided that the soft tissue is of small thickness compared to the planar dimension. In this sense, all the calibrated coupling effects of soft tissue on the FAS and SAS, obtained using transducers collocated at the interface of two phases, are comparable with the effects in real clinical settings where the transducers are placed on human soft tissues.

5.7. Compensation

The most prominent modulation exerted by the coupled soft tissues on the FAS and SAS has been observed to take place when the soft tissue is initially introduced. Such a modulation manifests as:

(i) As observed in Fig. 5 (velocity *vs.* thickness of the coupled soft tissue): a reduction in the velocity by approximately 10% for the FAS, and 23% for the SAS;
(ii) As observed in Fig. 7 (velocity *vs.* Young's modulus of the coupled soft tissue): a reduction in the velocity by about 11% for the FAS, and 22% for the SAS; and
(iii) Any further changes in the velocity as continuous increase in the thickness or elastic modulus of the coupled soft tissue are minute.

The above findings imply that surrounding soft tissues exert a perceptible influence on the velocity of both modes in a confined area only. These observations make it possible to apply the calibration results obtained in a specific state (*i.e.*, with a given thickness or given elastic properties of the soft tissue) to compensate for the effect of soft tissue coupling, regardless of differences in their thickness and elastic properties, if only the variations in wave velocity are used in a QUS exercise.

On the other hand, modulation from the soft tissue on the signal energy magnitude of the FAS or SAS is continuous with changes in thickness (Fig. 6) or elastic modulus (Fig. 8) of the surrounding soft tissue, accentuating that rectification of such coupling effect is case-dependent, if the variations in signal magnitude are also a parameter to be relied on in a QUS exercise. In that case, compensation for the coupling effect should be undertaken in terms of the calibrated relationships between the signal magnitude of FAS/SAS and soft tissue properties (Fig. 6 for different thicknesses; Fig. 8 for different elastic moduli).

The above calibration (Figs. 5–8) provides a rule of thumb for appropriate compensation, to a quantitative degree, for the coupling effect of soft tissues with different properties on propagation of the FAS and SAS. In this study, it has been demonstrated that the excitation frequency ranging from 50 to 200 kHz is suitable to generate guided waves in the presence of soft tissues, which can be conducive to clinical application of QUS.

6. Supplementary analysis using dedicated FE simulation

To facilitate understanding of the mechanism of the *in vitro* captured coupling effect, a dedicated FE modeling and simulation technique was developed using the commercial FE code ABAQUS®/EXPLICIT. In a synthesized bone phantom with an encastre boundary condition, both hard and soft phases were modeled using 3D elastic, homogeneous and isotropic eight-node brick elements. This modeling was warranted by three factors:

(i) During *in vitro* tests, a relatively low frequency (75 kHz) was adopted. As demonstrated elsewhere [31], the viscoelasticity of soft tissues is not a major concern when studying wave propagation if the frequency is less than 100 kHz; and under such a circumstance, the ASR layer can be treated as linear and elastic, although the influence of viscoelasticity of soft tissues has recently been reported [34];
(ii) Results from the compression testing, as shown in Fig. 2, indicated that the constitutive relationship of the fabricated ASR in this study had linear elastic properties; and
(iii) Earlier studies [9,14] have substantiated that the assumption of both bone and soft tissues being homogeneous and isotropic would not entail perceptible errors when canvassing ultrasound waves.

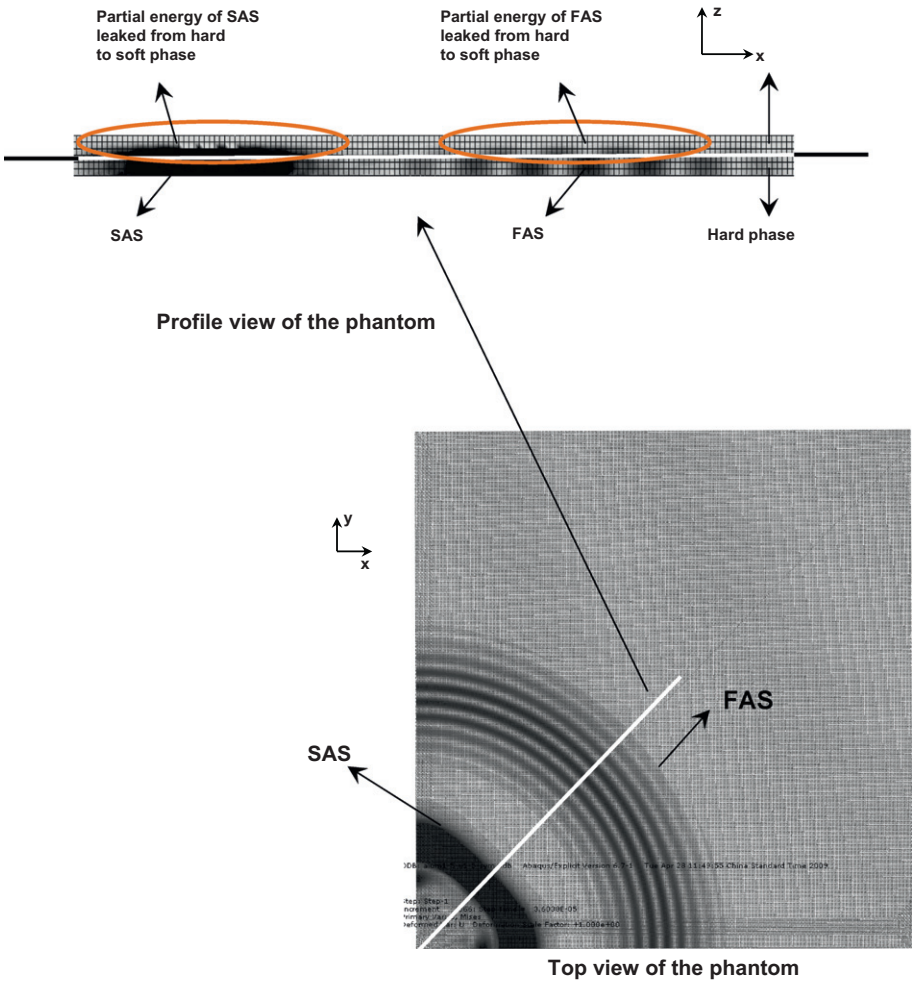

Fig. 13. Stress field as a result of wave propagation in phantom coupled with a layer of ASR, showing that energy associated with FAS and SAS leaks from hard to soft phase (the darker the greyscale the stronger the stress is; note: for convenience of comparison, the displayed stress field in the soft phase was multiplied by ten times; bottom figure: top-view of the phantom; top figure: profile along the white line in the bottom figure).

The interface between the hard and soft phases was simulated using a specialized surface-based coupling constraint in virtue of a node-to-surface formulation in ABAQUS®/EXPLICIT, named '*TIE*' [35]. This constraint connected the contacting surfaces of two phases and enforced the degree-of-freedom to be equal for the two contacting surfaces, one of which (that of the hard phase) was designated the master surface and the other (that of the soft phase) the slave surface. The transmitter and receiver were simulated using a pre-developed piezoelectric element model for numerical generation and acquisition of ultrasonic waves [1,36]. To ensure simulation accuracy, the largest dimension of FE elements in the model was set to be less than 1 mm, guaranteeing that at least ten elements were allocated per wavelengths of the FAS and SAS at 75 kHz.

With the above modeling and simulation, the stress field across the thickness of this two-phase phantom (when the ASR layer was 3.4 mm thick as an example) was obtained, as shown in Fig. 13, from which evident leakage of wave energy from hard to soft phase through the interface could be captured for both wave modes. The coupled ASR layer is a sort of soft substance supporting particulate motion patterns in both in-plane (for the FAS) and out-of-plane (for the SAS) dimensions, and it therefore provides a radiation path for both modes to leak into the overlying soft tissues. When leaky waves encounter the boundaries of different phases they are scattered and disseminate throughout the different phases. It is such energy leakage that accounts for the reduction in signal energy, as observed in Figs. 6 and 8.

7. An application: compensating for the coupling effect of soft tissue in QUS-based assessment of mimicked bone fracture

In clinical practice, monitoring of the healing progress of a fractured bone can be achieved using QUS, by detecting changes in either the FAS or the SAS in relation to baseline signals, as briefly described in Section 2. When QUS is conducted *in vivo* (in clinic), the coupling effect of surrounding soft tissues is ubiquitous but is often neglected, potentially leading to compromised or even erroneous assessment without proper rectification. In this section, as an application of the calibrated results presented above, the coupling effect is compensated for in an SAS-based QUS used for predicting the simulated healing status of a mimicked bone fracture, with the aim of improving the prediction precision.

Beforehand, to simulate fractured bone with different healing statuses, a set of seven samples was fabricated. In each sample, two identical acrylic plates ($230 \times 240 \times 3.2$ mm^3 each) were tied via an ASR strip (ASR strip was prepared in line with the fabrication steps listed in the Appendix) using the glue introduced in Section 4. The samples are sketched in Fig. 14a. All the ASR strips had an elastic modulus of 2.8 MPa, close to that of the callus in real fractured bones during their initial healing stage [37]. *Callus* is a substance in

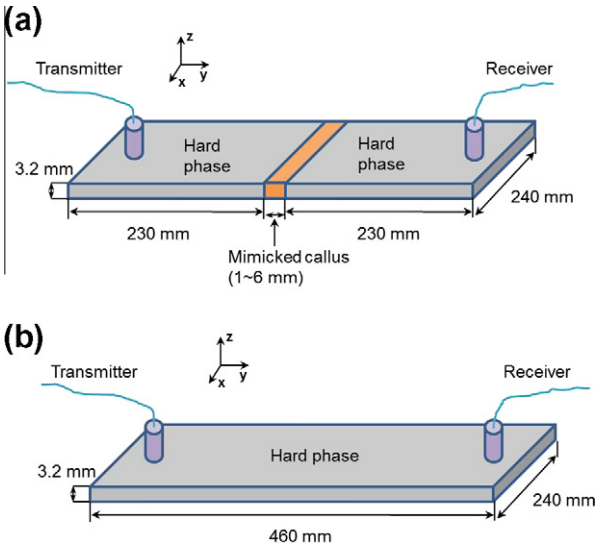

Fig. 14. Schematic of samples for QUS-based assessment of bone fracture: (a) with a callus, mimicking a fractured bone; and (b) without a callus, mimicking an intact bone (both cases neglecting the effect of ASR coupling).

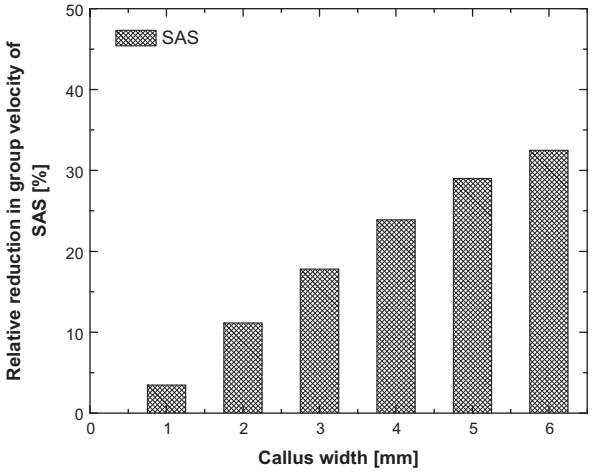

Fig. 15. Reduction in the propagation velocity of SAS *vs.* different callus widths (reflecting different healing stages) (note: correlation in this figure neglecting the effect of ASR coupling).

Table 2
Relative reduction in velocity of SAS *vs.* different callus widths (note: data in this table were obtained without considering the effect of ASR coupling).

Callus width (mm)	Relative reduction in propagation velocity of SAS (%)
0	0
1	3.5
2	11.1
3	17.8
4	23.9
5	29.0
6	32.5

the fractured region linking different bone fragments; at different stages of healing, callus has different dimensions and elastic properties, and therefore its geometric parameters (such as width) can be sensitive indicators of the healing progress of fractured bone. The ASR strips in the seven samples featured different widths (along the sample axial direction), from 0 to 6 mm with an increment of 1 mm, to mimic the callus in a fractured bone at different stages of healing (in particular, the width of 0 mm, as seen in Fig. 14b, corresponding to a healthy bone). A pair of transducers was placed atop each sample in terms of the axial transmission measurement. It should be noted that the authors had no intention of thoroughly exploring physiological issues related to bone healing (detailed discussion of bone healing can be found elsewhere [38,39]). This model was a simplified fracture model, developed with the aim of examining ultrasound wave propagation under the coupling effect of soft tissues. Although certain discrepancies from reality were present, this model has been demonstrated to be capable of accommodating the need to investigate ultrasound waves in a coupled system.

The SAS was employed, taking advantage of its shorter wavelength than that of FAS at a given excitation frequency. To generate the SAS, the transmitter was driven by five-cycle *Hanning*-windowed sinusoidal tonebursts at a central frequency of 100 kHz with a magnitude of 180 $V_{p\text{-}p}$ through the signal generation/acquisition system detailed in Section 5.1. The current selection of 100 kHz ensured the wave mode dominance of the SAS according to Fig. 10, as explained in Section 5.5, which also fell in the frequency range most commonly adopted in clinical QUS applications [20,33].

As demonstrated previously, fracture modulates ultrasound waves in bones, leading to a reduction in propagation velocity, which can be inversely used to predict healing progress of the fracture. Using the experimental method described in Section 5.1, reductions in velocity of the SAS for callus of different widths (1–6 mm, Fig. 14a), with regard to the velocity of the SAS in the healthy state (0 mm callus, Fig. 14b) were obtained, as shown in Fig. 15 and Table 2. The velocity of the SAS is reduced to different degrees when the callus is of different widths; the smaller the width (smaller callus width indicating that the fractured bone is developing toward a healthier status), the less the reduction.

Note that the correlations in Fig. 15 and data in Table 2 were obtained using the configuration shown in Fig. 14, without considering any coupled soft tissues. This is reflective of clinical reality (in many clinical applications, such relationships are often used directly for predicting the healing progress of bone fracture, neglecting the coupling effect). Further, to mimic an *in vitro* condition in which the coupling effect of soft tissues exists, a layer of ASR ($160 \times 60 \times 3.4$ mm^3; $E_{ASR} = 11.96$ kPa) was adhered to an arbitrarily selected sample among the seven, as illustrated in Fig. 16a. This sample thereafter served as an *in vitro* case with unknown healing status to be predicted (without knowledge of the callus width). A transducer pair was positioned at the interface between the hard and soft phases, clamping the ASR along the axial direction. The signal captured under that configuration (with callus of unknown width and coupled soft tissues) was considered the *in vitro* signal. The velocity of the SAS accordingly determined from the *in vitro* signal was denoted by $V^{(\text{Fig. 16(a)})}_{fracture-with\ ASR\ (in\ vitro)}$. It is noteworthy that, in terms of the conclusion drawn in Section 5.6, $V^{(\text{Fig. 16(a)})}_{fracture-with\,ASR\,(in\ vitro)}$ captured under the current configuration, Fig. 16a, was the same as that measured when the transducers were put atop the soft tissues (*in vivo* conditions in clinic).

7.1. Without compensation for effect of ASR coupling

Fig. 17 shows the comparison between the signal captured under the *in vitro* configuration (Fig. 16a) and the signal captured under the intact condition (Fig. 16b, a sample with neither the callus nor coupled ASR), from which the relative reduction in the velocity of SAS, $R_{in\ vitro-intact}$, was determined to be 23% (*i.e.*, $R_{in\ vitro-intact} = \frac{V^{(\text{Fig. 16(b)})}_{no\ fracture-without\ ASR} - V^{(\text{Fig. 16(a)})}_{fracture-with\ ASR\ (in\ vitro)}}{V^{(\text{Fig. 16(b)})}_{no\ fracture-without\ ASR}} = 23\%$, where $V^{(\text{Fig. 16(b)})}_{no\ fracture-without\ ASR}$ is the velocity of the SAS in an intact condition

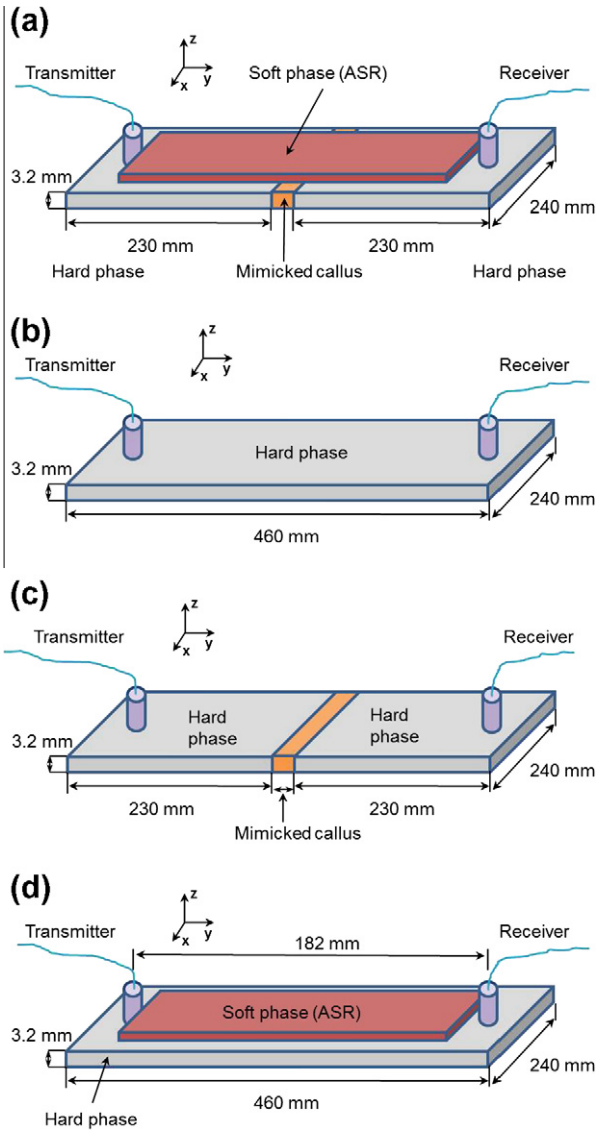

Fig. 16. Schematic of samples (a) with callus (unknown width, to be predicted) and coupled ASR layer, mimicking an *in vitro* case; (b) with neither callus nor coupled ASR layer, mimicking an intact case without overlying soft tissues; (c) with callus but without coupled ASR layer, mimicking a fractured bone without overlying soft tissues, and (d) without callus but with coupled ASR layer, mimicking an intact case with overlying soft tissues.

with no ASR coupling). Without considering the coupling effect of soft tissues, that reduction of 23% was attributed entirely to the existence of callus in the fractured bone sample. Based on the relationship between the reduction in velocity of the SAS and callus width (Fig. 15), the callus in the current healing status was predicted to be 4 mm in width, considerably different from the actual callus width of 2 mm.

7.2. With compensation for effect of ASR coupling

The above erroneous prediction echoes the earlier inference that, aside from the degradation in bone (*e.g.*, callus), the coupling effect of overlying soft tissues also contributes a certain amount of reduction in the velocity of the SAS. That effect should be compensated for properly before using Fig. 15 to predict the callus width, because the correlation displayed in Fig. 15 was established without considering any overlying soft tissues (in other words, Fig. 15

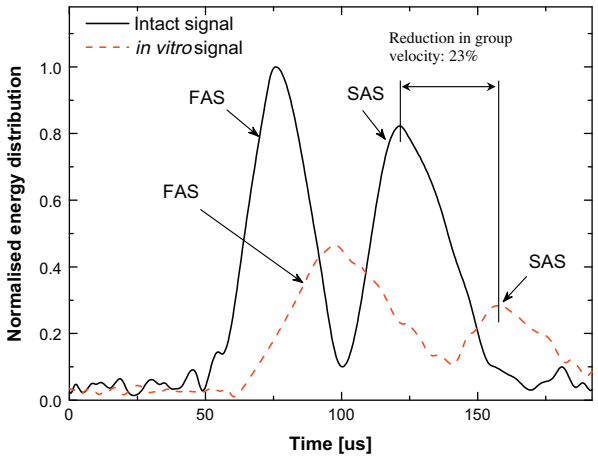

Fig. 17. Comparison of HT-processed results of signals captured from an intact sample (Fig. 16b) and from an mimicked fractured bone sample (*in vitro* case, Fig. 16a).

was obtained using the sample sketched in Fig. 16c with different callus widths).

Previously, it was calibrated (in Section 5) that the effect of soft tissue coupling causes a reduction in velocity of the SAS, even in an intact sample (the case in Fig. 16d). The relative reduction, with regard to an intact sample without any coupled ASR (Fig. 16b), is

$$\Gamma_{due\ to\ coupling} = \frac{V^{(\text{Fig. 16(b)})}_{no\ fracture-without\ ASR} - V^{(\text{Fig.16(d)})}_{no\ fracture-with\ ASR}}{V^{(\text{Fig. 16(b)})}_{no\ fracture-without\ ASR}}, (\text{for an intact case}) \tag{3a}$$

where $\Gamma_{due\ to\ coupling}$ is the relative reduction in the velocity of the SAS in an intact sample fully due to the coupling effect. $V^{(\text{Fig. 16(d)})}_{no\ fracture-with\ ASR}$ is the velocity of the SAS in the intact sample with a coupled ASR layer, the case shown in Fig. 16d.

Similarly, for a fractured sample, we have

$$\Gamma'_{due\ to\ coupling} = \frac{V^{(\text{Fig. 16(c)})}_{fracture-without\ ASR} - V^{(\text{Fig. 16(a)})}_{fracture-with\ ASR\ (in\ vitro)}}{V^{(\text{Fig. 16(c)})}_{fracture-without\ ASR}}, (\text{for a fractured case}) \tag{3b}$$

where $\Gamma'_{due\ to\ coupling}$ is the relative reduction in velocity of the SAS in a fractured sample fully due to the coupling effect; $V^{(\text{Fig. 16(c)})}_{fracture-without\ ASR}$ is the velocity of the SAS in the fractured sample with no coupled ASR layer, the case sketched in Fig. 16c.

Focusing on the *in vitro* sample to be evaluated (Fig. 16a), because the callus width was much smaller than the axial dimension of the sample, the coupling effect of overlying soft tissues on waves propagating within the callus region is negligible (note: only within the callus). This means that the overall coupling effect of soft tissues on the SAS in the entire fractured sample (Fig. 16a) can be equivalent to the effect exerted by the same soft tissues in the intact sample (Fig. 16d), namely

$$\Gamma_{due\ to\ coupling} = \Gamma'_{due\ to\ coupling} = \Gamma. \tag{4}$$

On the other hand, by referencing the calibration results of ASR coupling on the SAS, shown in Fig. 9, which was obtained using the same sample as that in Fig. 16d, Γ was determined to be 12% at the current excitation frequency of 100 kHz. Combining Eqs. (3) and (4), in addition to the prior knowledge (from Fig. 17) that

$$R_{in\ vitro-intact} = \frac{V^{(\text{Fig. 16(b)})}_{no\ fracture-without\ ASR} - V^{(\text{Fig. 16(a)})}_{fracture-with\ ASR\ (in\ vitro)}}{V^{(\text{Fig. 16(b)})}_{no\ fracture-without\ ASR}} = 23\%, \tag{5}$$

yields

$$\frac{V_{no\ fracture-without\ ASR}^{(\text{Fig. 16(b)})} - V_{fracture-without\ ASR}^{(\text{Fig. 16(c)})}}{V_{no\ fracture-without\ ASR}^{(\text{Fig. 16(b)})}} = \frac{R_{in\ vitro-intact} - \Gamma}{1-\Gamma}. \quad (6)$$

Observing the subscripts of the variables in the left-hand term of Eq. (6), all parameters could be obtained in the absence of a coupled ASR layer. These parameters were linked, through this equation, to the *in vitro* measurement condition in the presence of a coupled ASR layer, described by the right-hand term. This implies that the captured reduction in the velocity of the SAS was compensated for by taking into account the coupling effect of the ASR (*i.e.*, the coupling effect of overlying soft tissues was removed). Therefore, the relationship between the reduction in the velocity of the SAS and the variation in callus width (Fig. 15, which was established without considering any overlying soft tissues) can now be used to predict the callus width.

Substituting the measured relative reductions ($R_{in\ vitro-intact} = 23\%$ and $\Gamma = 12$) into Eq. (6), we have

$$\frac{V_{no\ fracture-without\ ASR}^{(\text{Fig. 16(b)})} - V_{fracture-without\ ASR}^{(\text{Fig. 16(c)})}}{V_{no\ fracture-without\ ASR}^{(\text{Fig. 16(b)})}} = \frac{R_{in\ vitro-intact} - \Gamma}{1-\Gamma} = \frac{23\% - 12\%}{1-12\%} = 12.5\%. \quad (7)$$

Interpolating 12.5% rather than 23% (used in Section 7.1) into Fig. 15, the callus width is now determined to be 2 mm, tallying with the real callus width.

8. Concluding remarks

With awareness that surrounding soft tissues can modulate the propagation characteristics of ultrasound waves in bones and potentially impair the precision of QUS-based bone assessment, the coupling effect arising from fabricated ASR on the FAS and SAS in synthesized bone phantoms was investigated ultrasonically and calibrated quantitatively. An *in vitro* testing series captured noticeable decreases in the propagation velocity and signal peak energy of both modes, in comparison with their counterparts in the same structures with no coupled soft tissues. The medium coupling impacts influence on different wave modes to different degrees. For both modes, the most significant changes occur when the ASR layer is initially introduced, and the decrease in signal peak energy continues with increase in the thickness or elastic modulus of ASR, but velocities fluctuate slightly regardless of further increase in ASR thickness or elastic modulus. It was also found that prediction of the healing progress of bone fracture based on changes in velocity of the FAS or the SAS might be inaccurate without taking into account the effect of soft tissue coupling. The calibrated effect was then applied to enhance the precision of SAS-based QUS when used for predicting the healing stage of a simulated bone fracture. By considering the coupling effect of soft tissues, the precision of QUS can be improved, stressing the necessity of considering and compensating for the coupling effect when performing QUS. Although the model described represents only coarse approximation of living tissues, the results indicate the need for further analysis of the propagation of ultrasound waves in a coupled system such as bone. Not only is the discussed coupling effect a concern in clinical QUS, but it is pervasive throughout generic engineering applications such as ultrasonic-wave-based NDE for submerged structures where surrounding fluid also modulates waves in structures. Thus the conclusions and observations arising from this study can also benefit relevant engineering applications.

Acknowledgments

The work was supported by a grant from the Research Grants Council of Hong Kong (Project No.: PolyU 527008) and grants from the Hong Kong Polytechnic University (Project No.: A-PK22 and A-PE1F).

Appendix A

ASRs of different elastic properties and geometries were prepared by controlling the proportions of silicone gel, firming agent and oil in the mixture, in accordance with the following steps:

(i) Mixing silicone gel (Wacker M4600A), firming agent (Wacker M4600B) and oil (AK35, all from Wacker Chemicals (Hong Kong) Ltd.) at a specific ratio: the ratio of firming agent to silicone gel (RFS) was kept at 0.1, while the ratio of oil to silicone gel (ROS) was varied from 0 to 2 with an increment of 0.2, resulting in different elastic moduli of the ASRs produced in a range from 536.51 to 2.89 kPa (the lower the ROS the higher the elastic modulus), as summarized in Table 1.
(ii) Keeping the mixture in a desiccator (DURAN Productions GmbH & Co. KG) which was then vacuumed using a pump (FY-1c, Feiyue Electrical Machinery Co., Ltd.) to maintain an interior pressure of 5 Pa. Air bubbles in the mixture were removed.
(iii) Injecting mixtures (in the form of liquid) into two molds, measuring $30 \times 30 \times 30\ mm^3$ and $160 \times 60 \times 40\ mm^3$, respectively. ASRs shaped with the former mold were used to determine their mechanical properties (compression testing in Fig. 1), and those shaped with the other mold were used for mimicking soft tissues, ready to be coupled with different hard phases; and
(iv) Keeping all mixtures in molds for 12 h allowing a curing process, to be trimmed to desired geometries.

ASRs of different thicknesses were made in line with the same procedures, in which the RFS and ROS were set at 0.1 and 1.6, respectively.

References

[1] J. Chen, Z. Su, L. Cheng, Identification of corrosion damage in submerged structures using fundamental anti-symmetric Lamb waves, Smart Mater. Struct. 19 (2010) 015004.
[2] J. Chen, J. Foiret, J.-G. Minonzio, M. Talmant, Z. Su, L. Cheng, P. Laugier, Measurement of guided mode wavenumbers in soft tissue–bone mimicking phantoms using ultrasonic axial transmission, Phys. Med. Biol. 57 (2012) 3025–3037.
[3] M.J.S. Lowe, Matrix Techniques for modelling ultrasonic waves in multilayered media, IEEE Trans. Ultrason. Ferr. 42 (1995) 525–541.
[4] M. Castaings, M. Lowe, Finite element model for waves guided along solid systems of arbitrary section coupled to infinite solid media, J. Acoust. Soc. Am. 123 (2008) 696–708.
[5] C.L. Yapura, V.K. Kinra, Guided waves in a fluid-solid bilayer, Wave Motion 21 (1995) 35–46.
[6] P.C. Yang, C.H. Norris, Y. Stavsky, Elastic wave propagation in heterogeneous plates, Int. J. Solids Struct. 2 (1966) 665–684.
[7] J.L. Rose, Ultrasonic Waves in Solid Media, second ed., Cambridge University Press, Cambridge, MA, 1999. pp. 126–128.
[8] J.D. Achenbach, Wave Propagation in Elastic Solids, North-Holland Pub. Co./American Elsevier Pub. Co., New York, 1984. pp. 326–344.
[9] P. Moilanen, P.H.F. Nicholson, V. Kilappa, S. Cheng, J. Timonen, Measuring guided waves in long bones: modeling and experiments in free and immersed plates, Ultrasound Med. Biol. 32 (2006) 709–719.
[10] P. Laugier, G. Haiat, Bone Quantitative Ultrasound, Springer, New York, 2011. pp. 147–179.
[11] P. Moilanen, M. Talmant, V. Kilappa, P. Nicholson, S.L. Cheng, J. Timonen, P. Laugier, Modeling the impact of soft tissue on axial transmission measurements of ultrasonic guided waves in human radius, J. Acoust. Soc. Am. 124 (2008) 2364–2373.

[12] R.M. White, S.W. Wenzel, Fluid loading of a Lamb-wave sensor, Appl. Phys. Lett. 52 (1988) 1653–1655.
[13] J.D.N. Cheeke, X. Li, Z. Wang, Observation of flexural Lamb waves (A0 mode) on water-filled cylindrical shells, J. Acoust. Soc. Am. 104 (1998) 3678–3680.
[14] J. Chen, Z. Su, L. Cheng, L. Qin, Influence of soft tissues on ultrasonic Lamb waves in synthesised soft tissue-bone phantoms, in: C.T. Lim, J.C.H. Goh (Eds.) 6th World Congress of Biomechanics (WCB 2010), Springer, Berlin, Heidelberg, Singapore, 2010. pp. 1315–1318.
[15] Y.P. Zheng, J. Chen, H.Y. Ling, Development of an ultrasound platform for the evaluation of plantar soft tissue properties: a feasibility study on silicone phantom feet, Instrum. Sci. Technol. 39 (2011) 248–260.
[16] S.H. Prins, H.L. Jørgensen, L.V. Jørgensen, C. Hassager, The role of quantitative ultrasound in the assessment of bone: a review, Clin. Physiol. 18 (1998) 3–17.
[17] S. Grondel, C. Paget, C. Delebarre, J. Assaad, K. Levin, Design of optimal configuration for generating A0 Lamb mode in a composite plate using piezoceramic transducers, J. Acoust. Soc. Am. 112 (2002) 84–90.
[18] P. Moilanen, Ultrasonic guided waves in bone, IEEE Trans. Ultrason. Ferr. 55 (2008) 1277–1286.
[19] M. Sasso, M. Talmant, G. Haiat, .S. Naili, P. Laugier, Analysis of the most energetic late arrival in axially transmitted signals in cortical bone, IEEE Trans. Ultrason. Ferr. 56 (2009) 2463–2470.
[20] K.I. Lee, S.W. Yoon, Feasibility of bone assessment with leaky Lamb waves in bone phantoms and a bovine tibia, J. Acoust. Soc. Am. 115 (2004) 3210–3217.
[21] P. Laugier, Instrumentation for in vivo ultrasonic characterization of bone strength, IEEE Trans. Ultrason. Ferr. 55 (2008) 1179–1196.
[22] P. Moilanen, P.H.F. Nicholson, T. Kärkkäinen, Q. Wang, J. Timonen, S. Cheng, Assessment of the tibia using ultrasonic guided waves in pubertal girls, Osteoporosis Int. 14 (2003) 1020–1027.
[23] S. Prevrhal, T. Fuerst, B. Fan, C. Njeh, D. Hans, M. Uffmann, S. Srivastav, H.K. Genant, Quantitative ultrasound of the tibia depends on both cortical density and thickness, Osteoporosis Int. 12 (2001) 28–34.
[24] E. Bossy, M. Talmant, M. Defontaine, F. Patat, P. Laugier, Bidirectional axial transmission can improve accuracy and precision of ultrasonic velocity measurement in cortical bone: a validation on test materials, IEEE Trans. Ultrason. Ferr. 51 (2004) 71–79.
[25] P. Wilcox, M. Lowe, P. Cawley, Omnidirectional guided wave inspection of large metallic plate structures using an EMAT array, IEEE Trans. Ultrason. Ferr. 52 (2005) 653–665.
[26] G. Lowet, G. Van der Perre, Ultrasound velocity measurement in long bones: measurement method and simulation of ultrasound wave propagation, J. Biomech. 29 (1996) 1255–1262.
[27] E. Camus, M. Talmant, G. Berger, P. Laugier, Analysis of the axial transmission technique for the assessment of skeletal status, J. Acoust. Soc. Am. 108 (2000) 3058–3065.
[28] X.N. Dong, X.E. Guo, The dependence of transversely isotropic elasticity of human femoral cortical bone on porosity, J. Biomech 37 (2004) 1281–1287.
[29] C.F. Njeh, J.R. Kearton, D. Hans, C.M. Boivin, The use of quantitative ultrasound to monitor fracture healing: a feasibility study using phantoms, Med. Eng. Phys. 20 (1999) 781–786.
[30] V. Egorov, S. Tsyuryupa, S. Kanilo, M. Kogit, A. Sarvazyan, Soft tissue elastometer, Med. Eng. Phys. 30 (2008) 206–212.
[31] M.L. Palmeri, A.C. Sharma, R.R. Bouchard, R.W. Nightingale, K.R. Nightingale, A finite-element method model of soft tissue response to impulsive acoustic radiation force, IEEE Trans. Ultrason. Ferr. 52 (2005) 1699–1712.
[32] Z. Su, L. Ye, Lamb wave propagation-based damage identification for quasi-isotropic CF/EP composite laminates using artificial neural algorithm: Part II – implementation and validation, J. Intel. Mater. Syst. Struct. 16 (2005) 113–125.
[33] A. Tatarinov, N. Sarvazyan, A. Sarvazyan, Use of multiple acoustic wave modes for assessment of long bones: model study, Ultrasonics 43 (2005) 672–680.
[34] S. Naili, M.-B. Vu, Q. Grimal, M. Talmant, C. Desceliers, C. Soize, G. Haïat, Influence of viscoelastic and viscous absorption on ultrasonic wave propagation in cortical bone: application to axial transmission, J. Acoust. Soc. Am. 127 (2010) 2262–2634.
[35] K.S. Hibbitt, Inc., ABAQUS User's Manual, version 6.2, 2001.
[36] Z. Su, L. Ye, Lamb wave propagation-based damage identification for quasi-isotropic CF/EP composite laminates using artificial neural algorithm: Part I – methodology and database development, J. Intel. Mater. Syst. Struct. 16 (2005) 97–111.
[37] V.C. Protopappas, I.C. Kourtis, L.C. Kourtis, K.N. Malizos, C.V. Massalas, D.I. Fotiadis, Three-dimensional finite element modeling of guided ultrasound wave propagation in intact and healing long bones, J. Acoust. Soc. Am. 121 (2007) 3907–3921.
[38] V.C. Protopappas, M.G. Vavva, D.I. Fotiadis, K.N. Malizos, Ultrasonic monitoring of bone fracture healing, IEEE Trans. Ultrason. Ferr. 55 (2008) 1243–1255.
[39] C.B. Machado, W.C.D. Pereira, M. Granke, M. Talmant, F. Padilla, P. Laugier, Experimental and simulation results on the effect of cortical bone mineralization in ultrasound axial transmission measurements: a model for fracture healing ultrasound monitoring, Bone 48 (2011) 1202–1209.